CrystEngComm

ROYAL SOCIETY OF CHEMISTRY

PAPER

View Article Online
View Journal | View Issue



Cite this: *CrystEngComm*, 2026, **28**, 2548

# Modulating some photophysical properties of cocrystals

Aloka A. Marasinghe, Boris B. Averkiev and Christer B. Aakeröy *

Received 22nd January 2026,
Accepted 15th March 2026

DOI: 10.1039/d6ce00063k

rsc.li/crystengcomm

In this study, nine cocrystals of *N*-(5-nitropyridin-2-yl)amide derivatives with 3-dimethylaminobenzoic acid (3DMABA) and 4-aminobenzoic acid (4ABA) were synthesized and structurally characterized in order to fine-tune photophysical properties by systematically modifying targets and coformers while maintaining overall structural consistency. The influence of competing factors, such as hydrogen-bonding motifs and steric effects, was examined through deliberate coformer selection and alkyl chain-length variation. The compounds exhibited visible color changes during grinding experiments, which were investigated using UV-visible spectroscopy and computational chemistry. The results show that changing the coformer can effectively modulate photophysical behavior while largely preserving crystal structure, and the competing intermolecular forces do not limit control over key solid-state structural parameters. Furthermore, the observed photophysical properties and colors can be rationalized and predicted based on calculated HOMO–LUMO gaps of donor–acceptor pairs, demonstrating a strategy for controlled design of functional cocrystals.



## Introduction

The characteristics of solid-state materials, such as thermal stability,[1–4] aqueous solubility,[5–7] mechanical flexibility,[8–12] and manufacturability,[13,14] determine performance and effectiveness when transitioning from fundamental research to applications and devices. The molecular building blocks of a crystalline material also impact its bulk properties, but the relative orientation of these building blocks with respect to each other can make a dramatic difference in physical properties. With this in mind, a range of bottom-up strategies have been employed to control solid-state assembly through the deliberate use of intermolecular forces such as hydrogen bonding,[15–18] halogen bonding,[19,20] chalcogen bonding,[21,22] and pi–pi interactions, *etc.* The outcomes of these strategies can lead to the formation of several new solid forms, including salts, polymorphs, hydrates, solvates, and cocrystals. The extent to which these forms can be made with a high degree of predictability is certainly debatable when it comes to solvates/hydrates and polymorphs, and salts can be constructed only from molecules that are inherently ionizable.

However, over the past two decades, the synthesis of organic cocrystals has attracted tremendous attention[23–26] from both academia and industry as a more versatile and robust avenue towards functional materials, owing to their ability to enhance physicochemical properties[27–32] in a modular fashion without affecting their inherent molecular characteristics. Therefore, cocrystal synthesis has become a versatile tool for improving properties such as stability,[33–37] solubility,[38–41] and mechanical flexibility.[42–44]

Cocrystals are typically synthesized through structure-directing non-covalent interactions, which play a crucial role in shaping both the structural and functional properties displayed by these materials.[45–48] In simpler terms, the way molecules interact with each other in multicomponent molecular solids, cocrystals, greatly influences cocrystal structure and behavior.[49] However, there are many other factors that also influence cocrystal formation, such as sterics, relative solubility, and kinetics of crystallization, *etc.*[50,51]

Recently, cocrystallization has emerged as an effective way to tune photophysical properties of solid-state materials. In 2020, Zeng and coworkers reported the color tuning of an active pharmaceutical ingredient *via* cocrystallization, presenting metronidazole and pyrogallol cocrystals as a case study.[52] In this study, the cocrystal showed an increased dissolution rate compared to the drug itself, and the results suggested that the cocrystal strategy may be used to tune the color of pharmaceutical drugs, which might help drug formulation development. A study by Wang and coworkers developed a color-tunable upconversion emission switch in which two different electron donors with the same acceptor molecule yield distinct red and yellow emissions, providing a good example of controlling cocrystal-to-cocrystal transformation.[53] MacGillivray and coworkers reported a red zwitterionic cocrystal of acetaminophen and 2,4-pyridinedicarboxylic acid, and despite both parent materials being colorless, the cocrystal exhibited a red color, which was due to reduced π–π gap based on density

*Department of Chemistry, Kansas State University, Manhattan, KS, 66506, USA. E-mail: aakeroy@ksu.edu*

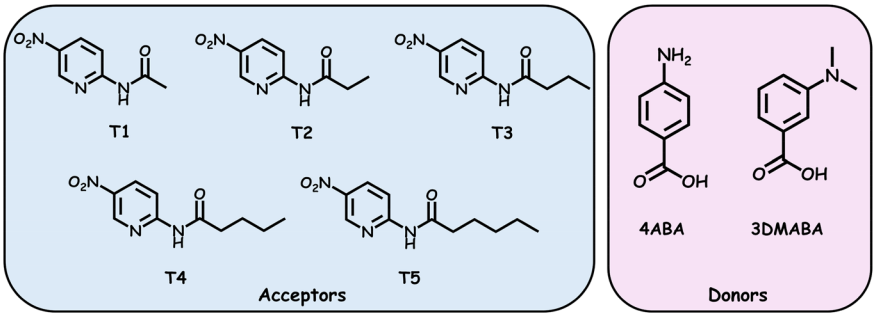


Fig. 1 Chemical structures of donor and acceptor molecules.

functional theory calculations.[54] Together, these studies suggest that cocrystallization is a powerful approach to modulate photophysical properties of solid-state materials.

Inspired by those studies, in this work we explored the possibility of fine-tuning photophysical properties in a series of cocrystals by making very specific changes to the nature of the coformers whilst keeping the overall crystal structures as constant as possible. We also examined the relative importance of competing factors in solid-state assembly such as hydrogen bonding and 'sterics' by increasing the chain length of our target material systematically, to maintain considerable control of the main structural parameters and metrics in these solids. With these two goals in mind, we synthesized nine cocrystals using five different acceptor molecules (targets) and two different donor molecules (coformers). The molecules are classified as 'donors' and 'acceptors' based on the role they are most likely to play in a charge-transfer scenario. Here, we chose 3-dimethylaminobenzoic acid (3DMABA), and 4-aminobenzoic acid (4ABA) as donors with different electron-donating capacities and *N*-(5-nitropyridin-2-yl)acetamide (T1), *N*-(5-nitropyridin-2-yl)propionamide (T2), *N*-(5-nitropyridin-2-yl) butyramide (T3), *N*-(5-nitropyridin-2-yl)pentanamide (T4), and *N*-(5-nitropyridin-2-yl)hexanamide (T5) as acceptors to set up a group of cocrystals (Fig. 1).

The choice of coformers was deliberate, and we expected the carboxylic acid functionality of the donors to form robust $R_2^2(8)$ dimeric hydrogen-bonding (Fig. 2) with the pyridine nitrogen and amide –NH of the acceptors; this heterosynthon is well established in the literature.[55–57] We intended for this to promote a certain amount of structural consistency across the series of cocrystals. If overall structural control can be achieved, we hypothesized that it would be possible to make deliberate changes to the photophysical behavior of these materials simply by referencing the calculated HOMO–LUMO gap of donor–acceptor pairs of molecules.

## Experimental section

All acceptor molecules were synthesized and purified in our laboratory.[58] Other precursors and solvents were purchased from commercial sources and used without further purification. Melting points were recorded on a TA Instruments DSC Q20 differential scanning calorimeter. IR spectra were recorded with a Nicolet 380 FT-IR spectrometer using an attenuated total reflection (ATR) technique and ZnSe as the crystal. Single-crystal X-ray diffraction (SCXRD) data were collected on a Rigaku XtaLAB Synergy-S single-crystal X-ray diffractometer equipped with Cu Kα radiation. PXRD patterns were collected using a Bruker X-ray powder diffractometer equipped with CuKα radiation, operated at 30 kV and 15 mA. Diffuse reflectance absorbance data were measured using a Cary 500 UV-vis-NIR spectrophotometer. HOMO–LUMO calculations were done with density functional B3LYP level of theory using 6-311++G** basis set in vacuum, using Spartan 14′ software.[59]

### Preparation of the cocrystals

Liquid-assisted grinding was performed with equimolar amounts of donor and acceptor in the presence of one or two drops of methanol. In each case, the FT-IR spectrum of the ground mixture was compared to those of the pure starting materials to confirm cocrystal formation. A solution of the ground mixture in a suitable solvent was then allowed to evaporate slowly for about one week to allow crystal formation.

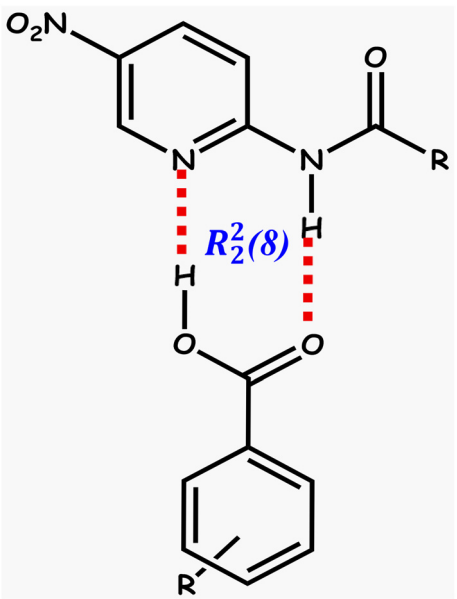


Fig. 2 Anticipated $R_2^2(8)$ dimeric hydrogen-bonding motif.

Table 1 Solvents used for crystal growth and crystal descriptions

| Compound | Code | Solvent | Color and morphology | Melting point/°C |
|---|---|---|---|---|
| *N*-(5-Nitropyridin-2-yl)propionamide + 3DMABA-polymorph I | **T2-3DMABA-PI** | Methanol | Light orange, plate | 121–123 °C |
| *N*-(5-Nitropyridin-2-yl)propionamide + 3DMABA-polymorph II | **T2-3DMABA-PII** | Dichloromethane | Orange, plate | 125–127 °C |
| *N*-(5-Nitropyridin-2-yl)butyramide + 3DMABA | **T3-3DMABA** | Methanol | Reddish orange, irregular block | 123–125 °C |
| *N*-(5-Nitropyridin-2-yl)pentanamide + 3DMABA | **T4-3DMABA** | Methanol | Orange, irregular block | 140–142 °C |
| *N*-(5-Nitropyridin-2-yl)hexanamide + 3DMABA | **T5-3DMABA** | Methanol | Orange, plate | 123–125 °C |
| *N*-(5-Nitropyridin-2-yl)propionamide + 4ABA | **T2-4ABA** | Ethyl acetate | Light yellow, needle | 154–156 °C |
| *N*-(5-Nitropyridin-2-yl)butyramide + 4ABA | **T3-4ABA** | Methanol | Yellow, irregular | 161–164 °C |
| *N*-(5-Nitropyridin-2-yl)pentanamide + 4ABA | **T4-4ABA** | Methanol | Yellow, plate | 141–144 °C |
| *N*-(5-Nitropyridin-2-yl)hexanamide + 4ABA | **T5-4ABA** | Methanol | Light yellow, needle | 121–123 °C |

Table 2 Crystallographic data

| Structure | Space group | $Z$, $Z'$ | $a$/Å | $b$/Å | $c$/Å | $U_{cell}$/Å$^3$ | $T$/K | $D_{calc}$/g cm$^{-3}$ (at $T$) |
|---|---|---|---|---|---|---|---|---|
| **T2-3DMABA-PI** | $P2_1/n$ | 4,1 | 16.7360(4) | 4.91439(11) | 21.9254(5) | 1784.68(7) | 200.00(10) | 1.341 |
| **T2-3DMABA-PII** | $C2/c$ | 8,1 | 24.8829(8) | 6.1032(2) | 23.3288(12) | 3484.7(2) | 295.0(4) | 1.374 |
| **T3-3DMABA** | $P\bar{1}$ | 2,1 | 6.21761(15) | 12.5048(2) | 12.7578(4) | 945.96(4) | 200.0(1) | 1.314 |
| **T4-3DMABA** | $P\bar{1}$ | 2,1 | 6.35274(15) | 12.46903(18) | 12.9378(3) | 966.16(4) | 200(2) | 1.335 |
| **T5-3DMABA** | $P\bar{1}$ | 2,1 | 6.42159(9) | 12.65205(14) | 13.02701(17) | 992.29(2) | 200.00(10) | 1.347 |
| **T2-4ABA** | $P2_1/n$ | 4,1 | 12.5882(2) | 5.17490(7) | 23.3666(4) | 1521.34(4) | 200.00(10) | 1.451 |
| **T3-4ABA** | $P\bar{1}$ | 2,1 | 5.8059(4) | 11.8005(10) | 12.9057(16) | 823.35(14) | 200.00(10) | 1.397 |
| **T4-4ABA** | $P\bar{1}$ | 2,1 | 6.15171(12) | 12.3495(4) | 12.6749(4) | 892.97(4) | 295.9(3) | 1.340 |
| **T5-4ABA** | $P2_1/n$ | 4,1 | 20.1578(5) | 4.90086(14) | 32.5043(9) | 3210.75(15) | 297(1) | 1.265 |

No cocrystals incorporating T1 were formed; on the other hand, two polymorphs of the T2-3DMABA cocrystals were formed. Details concerning these cocrystals formed by this procedure are presented in Table 1.

Selected crystallographic data are summarized in Table 2, while complete experimental details are given in the SI. The structures were solved with the ShelXT 2018/2 (ref. 60) structure solution program using the Intrinsic Phasing solution method, and Olex2 (ref. 61) was used as the graphical interface. The model was refined with version 2018/3 of ShelXL 2018/3 (ref. 62) using Least Squares minimization.

### Solid-state replacement studies

Solid-state replacement experiments were carried out to evaluate the possibility of coformer exchange in the pre-formed cocrystals. The isolated cocrystal was mixed with the second, and potentially disruptive, coformer in two different stoichiometric ratios (1 : 0.5 and 1 : 1 relative to the original coformer composition), and the mixtures were subjected to liquid-assisted grinding (LAG). The resulting products were analyzed by PXRD and compared with PXRD patterns of the starting cocrystals and the corresponding starting materials to determine whether coformer exchange had occurred.

## Results and discussion

### Physical appearance

All the starting targets and coformers utilized in this study appeared as white or off-white powders. However, noticeable color changes occurred during the grinding studies, as depicted in Fig. 3. It should be noted that none of the grinding experiments with T1 produced any cocrystals, based on our IR analysis, and neither of the ground mixtures of T1 gave any obvious color changes.

All cocrystals that were formed with T2–T5 displayed distinctly different physical appearances, Fig. 4, compared to their respective starting materials.


Fig. 3 Physical appearance of starting materials; T3, 3DMABA, 4ABA, and their ground mixtures.

 

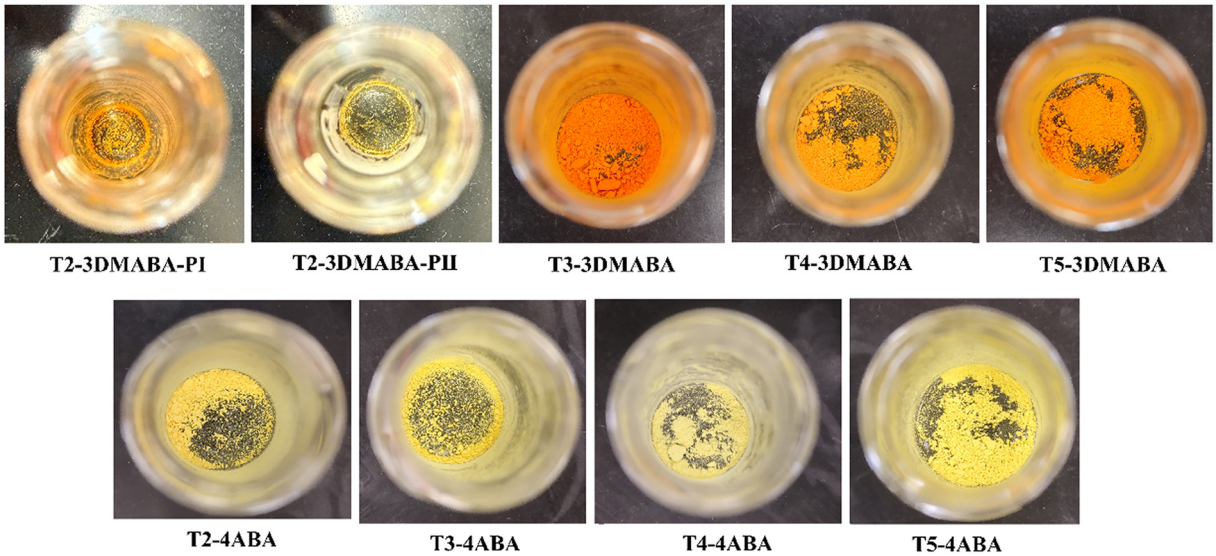


Fig. 4 Physical appearance of resultant ground mixtures.

## Infrared spectra (IR) analysis

To confirm the formation of cocrystals, the IR spectra of acceptors, donors, and ground mixtures were analyzed. The characteristic peaks of all five acceptors, two donors, and ground mixtures are given in Table 3.

In the IR spectrum of each cocrystal, the characteristic peaks have shifted significantly from their original positions. However, for the T1 acceptor with both 3DMABA and 4ABA, the coformer peak remained in the same place, indicating no cocrystal formation.

In the 3DMABA coformer, the C═O stretching vibration peak is observed at 1670 $cm^{-1}$, while in the 4ABA coformer it is located at 1660 $cm^{-1}$. The C═O stretching vibration peaks of the four ground mixtures, T2-3DMABA, T3-3DMABA, T4-3DMABA, and T5-3DMABA, corresponding to the 3DMABA donor, exhibit a blue shift, at 1672, 1675, 1679, and 1679 $cm^{-1}$, respectively. In these four grindings, the C═O peak accountable for acceptors, T2, T3, T4, and T5, are also blue shifted at 1705, 1712, 1714, and 1712 $cm^{-1}$, respectively.

As with the ground mixtures of the 3DMABA coformer, the four ground mixtures of the 4ABA coformer exhibit a blue shift for donor C═O, at 1672, 1675, 1674, and 1686 $cm^{-1}$, respectively. In these four cocrystals, the C═O peaks accountable for targets T2, T3, and T4 are also blue shifted at 1707, 1706, and 1715 $cm^{-1}$, respectively, except the C═O peak for T5. For T5-4ABA, the C═O peak belonging to T5 is red-shifted to 1695 $cm^{-1}$, confirming the formation of a different type of cocrystal.

In summary, significant shifts of the position of the C═O stretching mode were taken as evidence for cocrystal formation.

Table 3 IR frequencies of acceptors, donors and ground mixtures

| | | Coformer | |
|---|---|---|---|
| | | 3DMABA | 4ABA |
| Target | IR stretch/$cm^{-1}$ | **1670** | **1660** |
| **T1** | **1685/1669** | 1678/1670 | 1672/1662/1656 |
| **T2** | **1682** | 1705, 1672 | 1707, 1672 |
| **T3** | **1695** | 1712, 1675 | 1706, 1675 |
| **T4** | **1697** | 1714, 1679 | 1715, 1674 |
| **T5** | **1697** | 1712, 1679 | 1695, 1686 |

## Crystal structure analysis

We obtained crystals suitable for single-crystal X-ray diffraction for nine cocrystals (T2-3DMABA-PI, T2-3DMABA-PII, T3-3DMABA, T4-3DMABA, T5-3DMABA, and T2-4ABA, T3-4ABA, T4-4ABA, T5-4ABA). In all but one compound, there is a 1 : 1 stoichiometric ratio of the donor and acceptor molecules. The one exception is T5-4ABA, where the donor : acceptor ratio is 1 : 2. In addition, T2-3DMABA produced two polymorphs, crystallized from methanol and dichloromethane, Table 1.

The polymorph structures that formed with T2 belonged to $P2_1/n$ and $C2/c$ space groups in the monoclinic system. The T3-3DMABA, T4-3DMABA, and T5-3DMABA cocrystals exhibit a similar packing arrangement to each other, which belongs to the triclinic, $P\bar{1}$ space group, Fig. 5.

All donor and acceptor molecules of cocrystals are stacked in a slipped face-to-face arrangement, facilitating charge-transfer between adjacent π clouds. Charge-transfer is indicated by relatively short interplanar distances 3.171 Å for T2-3DMABA-PI, 3.324 Å for T2-3DMABA-PII, 3.337 Å for T3-3DMABA, 3.345 Å for T4-3DMABA, and 3.299 Å for T5-3DMABA (Fig. S1–S5, SI) leading to colored compounds. The donor and acceptor of each cocrystal are interconnected through C═O···H–N and O–H···N(py) hydrogen bonds (Fig. 4(a)i–(c)i).

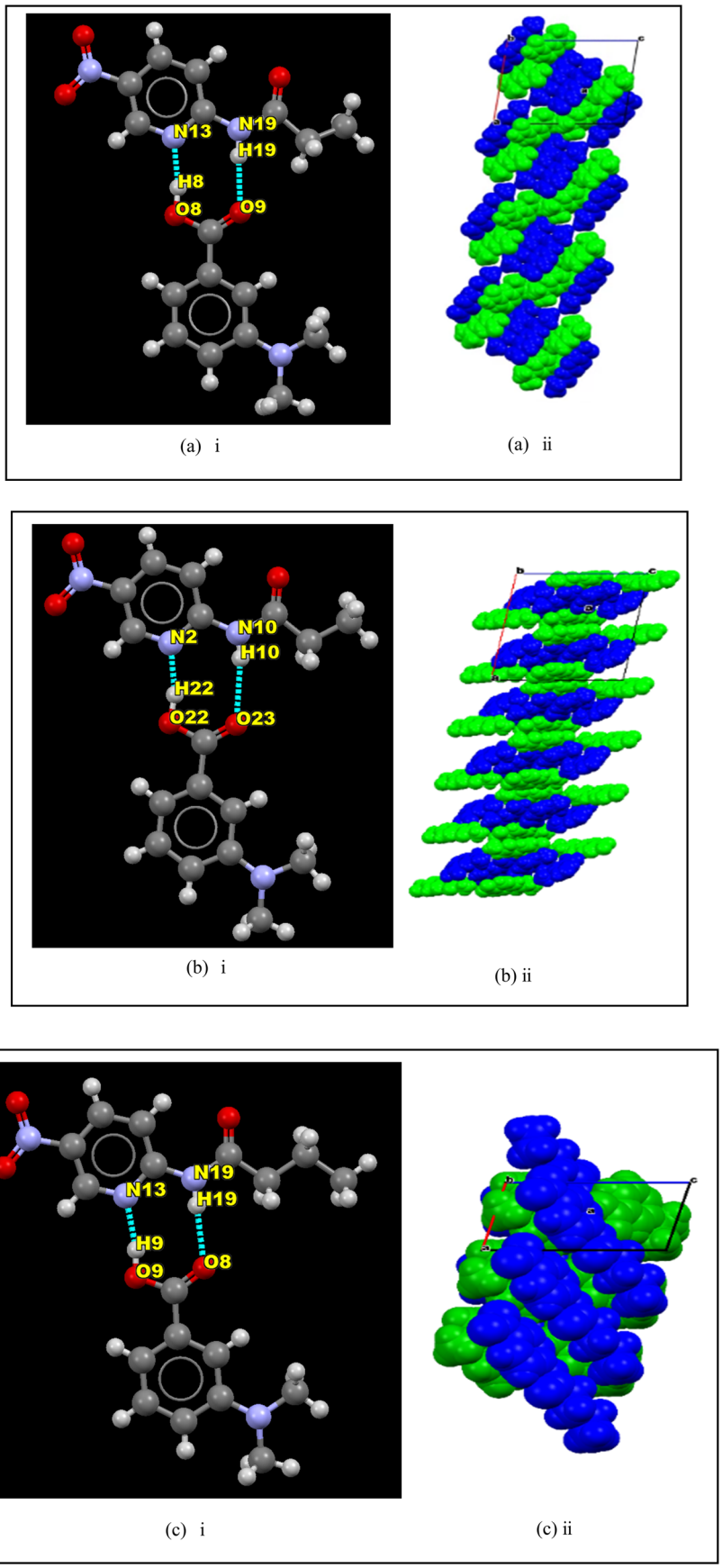


**Fig. 5** (a) i. Asymmetric unit of T2-3DMABA-PI, (a) ii. π···π stacking, (b) i. asymmetric unit of T2-3DMABA-PII, (b) ii. π···π stacking, (c) i. asymmetric unit of T3-3DMABA, (c) ii. π···π stacking (blue = donor, green = acceptor).

 

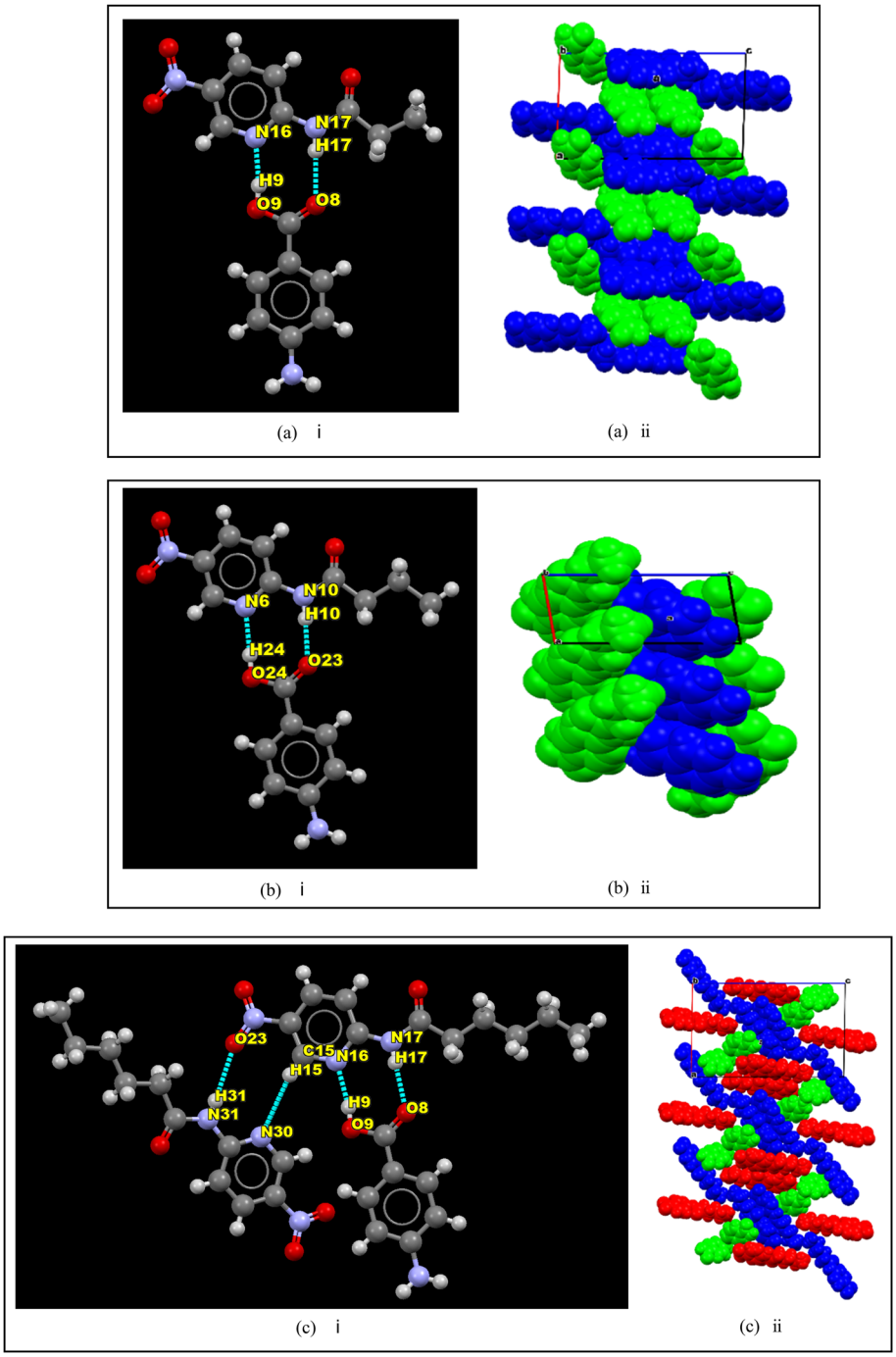


**Fig. 6** (a) i. Asymmetric unit of T2-4ABA, (a) ii. π···π stacking (blue = donor, green = acceptor), (b) i. asymmetric unit of T3-4ABA-PII, (b) ii. π···π stacking (green = donor, blue/red = acceptors), (c) i. asymmetric unit of T5-4ABA, (c) ii. Charge-transfer structure.

In the series with 4ABA coformer, the cocrystals belonged to two different space groups, $P2_1/n$ and $P\bar{1}$. T2-4ABA and T5-4ABA belong to the $P2_1/n$ space group in the monoclinic system, and T3-4ABA and T4-4ABA belong to the $P\bar{1}$ space group in the triclinic system. In each case, acceptor and donor appear in a 1 : 1 stoichiometric ratio except for the one with the T5 target, where they interact in a 2 : 1 acceptor : donor ratio, Fig. 6. Although T2-4ABA and T5-4ABA belong to the same space group, the packing arrangement is different since the molar ratios are different. In the first three cocrystals, the layers are weakly connected with a face-to-face pattern leading to charge-transfer interaction, but the last one was completely different (interlayer distances: 3.237 Å for T2-4ABA, 3.175 Å for T3-4ABA, 3.277 Å for T4-4ABA, and 3.355 Å for T5-4ABA) (Fig. S6–S9, SI).

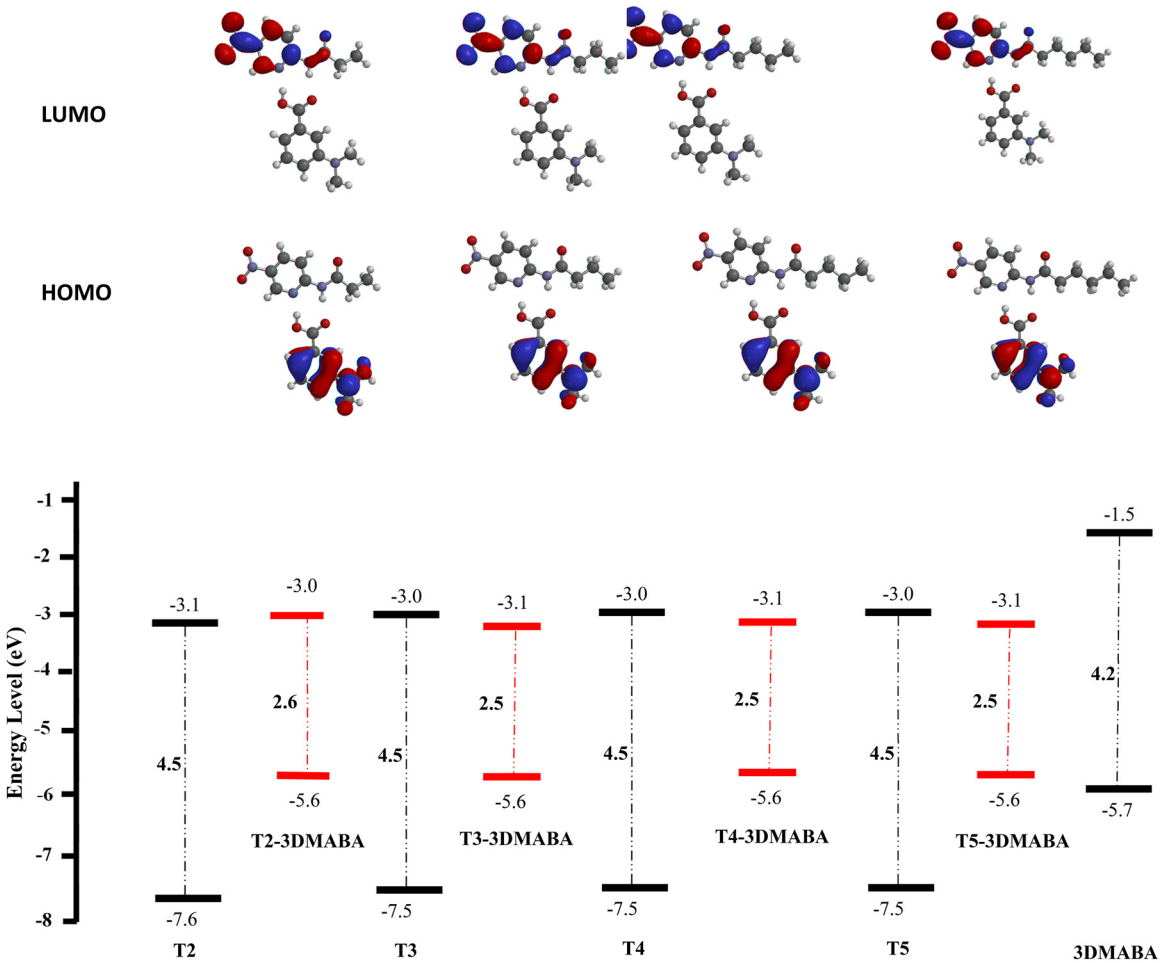


Fig. 7 HOMO and LUMO energy level diagrams of 3DMABA cocrystals and their starting materials.

### Powder X-ray diffraction (PXRD) analysis

In order to establish phase purity of the cocrystals, the PXRD patterns of the acceptor, donors, and ground mixtures were analyzed. The simulated PXRD patterns of the nine cocrystals were generated using Mercury[63] and compared with the experimental PXRD patterns of the ground mixtures (SI). The PXRD patterns of the cocrystals are different from those of the individual donors and acceptors, suggesting the formation of new crystalline phases. Furthermore, the diffraction peak positions in the experimental PXRD patterns of the six cocrystals (T3-3DMABA, T4-3DMABA, T5-3DMABA, T2-4ABA, T3-4ABA, and T4-4ABA) and the simulated PXRD patterns are consistent with each other, without the presence of additional peaks, underscoring that these powders are structurally homogenous. However, the simulated and experimental PXRD patterns of T2-3DMABA and T5-4ABA are different and also unrelated to their donor and acceptor PXRD patterns, respectively, indicating possible polymorphism (which was separately confirmed for T2-3DMABA in our single-crystal X-ray studies).

### HOMO–LUMO calculations

Frontier molecular orbital theory can provide valuable insights into the photophysical properties of charge-transfer compounds. To explore whether it is possible to correlate the observed photophysical properties of these cocrystals with the calculated HOMO–LUMO energy gap, we carried out the relevant DFT calculations at the B3LYP/6-311++G** level of theory in vacuum using Spartan to determine the energy levels of donors and acceptors separately, as well as for the heteromeric donor–acceptor pairs. (Fig. 6 and 7). Donor and acceptor molecules display wide HOMO–LUMO gaps with values of 4.2 eV for 3DMABA, 4.9 eV for 4ABA, and 4.5 eV for all four target molecules. When the cocrystals are formed, the HOMO–LUMO gaps are narrowed. The energy gap values [$E_{LUMO} - E_{HOMO}$] of T2-3DMABA, T3-3DMABA, T4-3DMABA, T5-3DMABA, T2-4ABA, T3-4ABA, T4-4ABA, and T5-4ABA are 2.6 eV, 2.5 eV, 2.5 eV, 2.5 eV, 3.3 eV, 3.3 eV, 3.3 eV, 3.5 eV, and 3.1 eV, respectively. This narrowing facilitates the charge-transfer between donor and acceptor molecules. As shown in Fig. 7 and 8, the HOMOs of the four cocrystals are located on the corresponding donors, and the LUMOs are distributed on the acceptors. It further confirms that

 

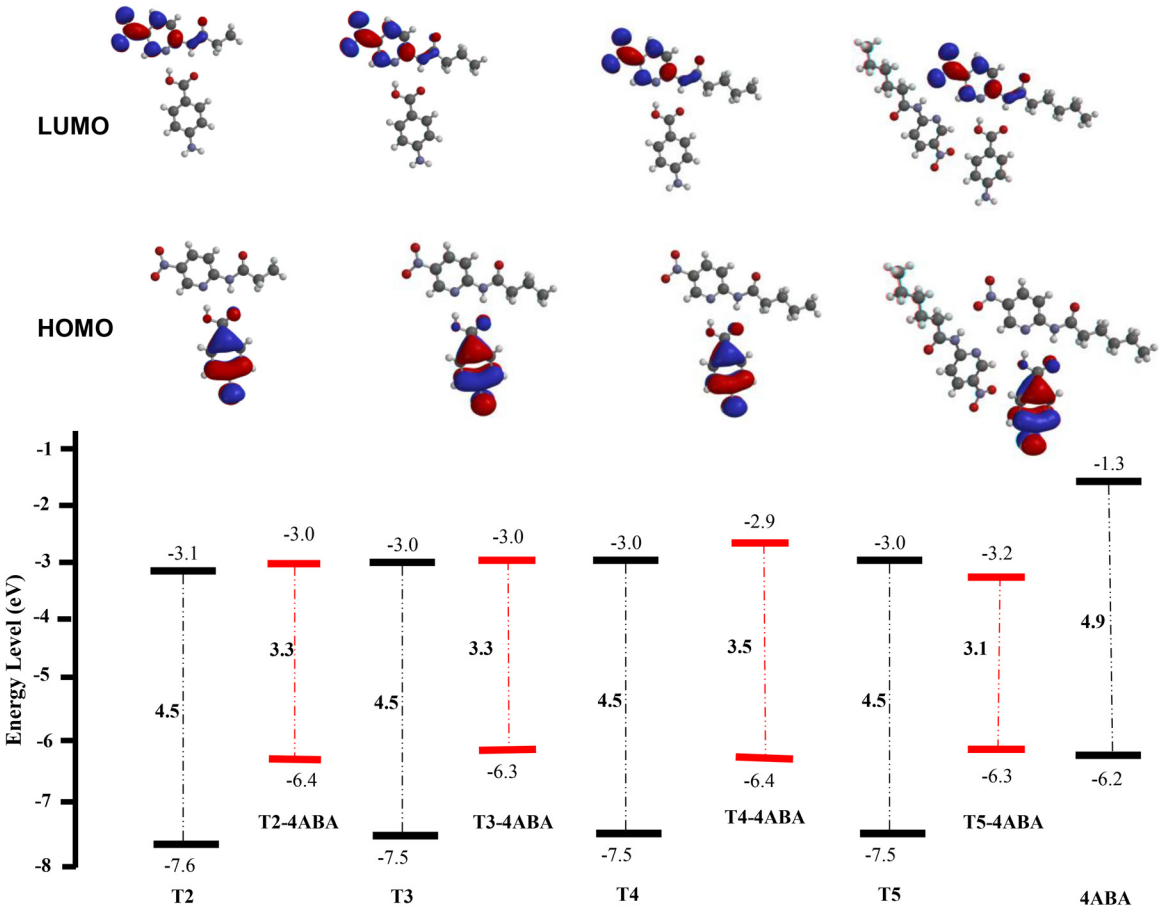


Fig. 8 HOMO and LUMO energy level diagrams of 4ABA cocrystals and their starting materials.

the charge-transfer transitions take place from donors to acceptors. Moreover, the colors of the materials aligned effectively with the resultant energy gaps.

### Charge transfer character

The optical properties and electronic transitions for T3-3DMABA and T3-4ABA were further investigated using TD-DFT calculations at the B3LYP/6-31G level of theory in vacuum using Gaussian. The calculated electronic absorption spectrum of T3-3DMABA exhibits two low-energy transitions at 679 nm (S1) and 676 nm (S2), and each is composed of multiple electronic transitions. The oscillator strengths of these transitions are 0.0064 a.u. and 0.0343 a.u., respectively. Therefore, it can be concluded that this absorption peak is dominated by the excitation at 676 nm.

Similarly, the electronic absorption spectrum of T3-4ABA was calculated at the same level of theory. Two low-energy transitions were observed at 487 nm (S1) and 486 nm (S2), with oscillator strengths of 0.0028 a.u. and 0.0029 a.u., respectively. Since the oscillator strengths are nearly identical, both transitions contribute similarly to the absorption spectrum. Analysis of the molecular orbital contributions shows that the first excited state (S1, 487 nm) arises from a combination of HOMO → LUMO+1 and HOMO−1 → LUMO transitions, while the second excited state (S2, 486 nm) involves HOMO−1 → LUMO+1 and HOMO → LUMO+1 transitions. These results indicate that both states have comparable transition probabilities, leading to similar intensities in the calculated spectrum. The transitions and their contributions are given in Fig. 9 and Table 4.

### Photophysical properties

**Solid-state UV absorption.** Solid-state UV absorption spectra of the acceptors, donors, and cocrystals were obtained to investigate the photophysical properties of the cocrystals (Fig. 10 and SI). Acceptor molecules exhibit absorption peaks within the range of 300–420 nm, while 3DMABA shows the absorption around 350–450 nm, and 4ABA has a strong absorption within 325–350 nm. In particular, the absorption peaks of cocrystals with 3DMABA coformers exhibit a wide range of absorbance within 400–600 nm, and the cocrystal with 4ABA coformer shows a broad range of absorbance within 400–500 nm. The absorption peaks of the acceptor and the donor molecules can be attributed to the π → π* transition of the conjugated structure. Moreover, the absorption bands of all nine cocrystals display broadening and red-shift, clearly indicating the occurrence of charge-transfer between the acceptor and the donor molecules within the cocrystals.

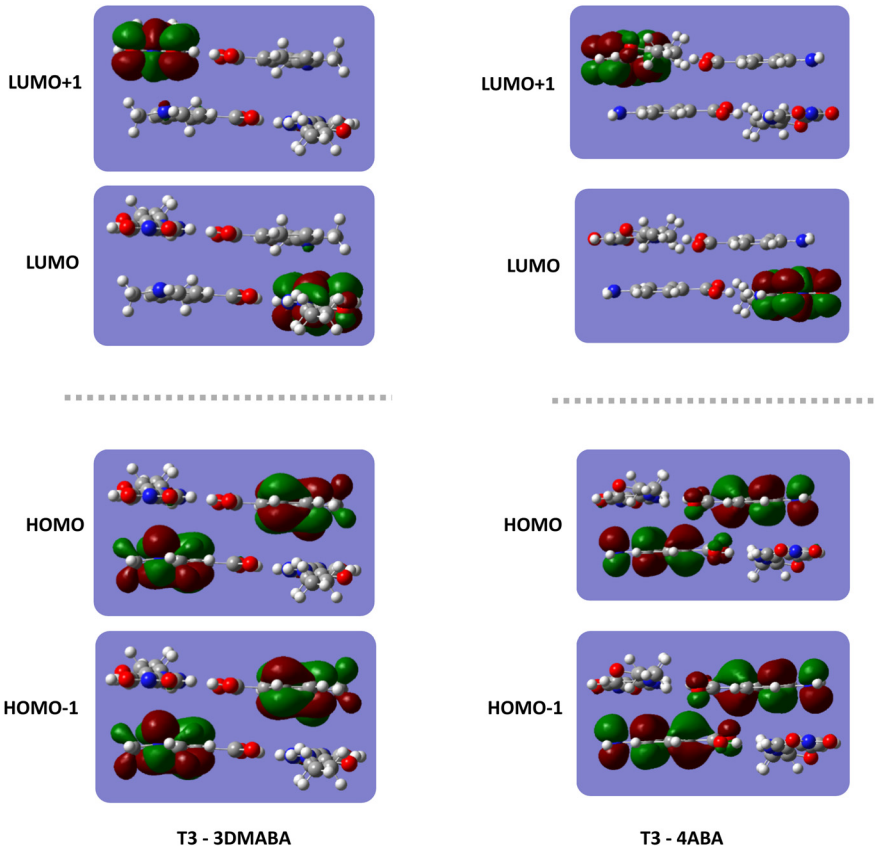


Fig. 9 Molecular orbitals contributing to the transitions.

Table 4 Calculated electronic absorption parameters

| Compound | Excitation energy/eV | Excited state | Oscillator strength (a.u) | Transitions | Weight |
|---|---|---|---|---|---|
| T3-3DMABA | 1.8255 (679 nm) | 1 | 0.0064 | HOMO−1 → LUMO | 21.03% |
| | | | | HOMO−1 → LUMO+1 | 3.83% |
| | | | | HOMO → LUMO | 22.08% |
| | | | | HOMO → LUMO+1 | 2.95% |
| | 1.8334 (676 nm) | 2 | 0.0343 | HOMO−1 → LUMO | 0.04% |
| | | | | HOMO−1 → LUMO+1 | 19.75% |
| | | | | HOMO → LUMO | 2.7% |
| | | | | HOMO → LUMO+1 | 23.36% |
| T3-4ABA | 2.5461 (487 nm) | 1 | 0.0028 | HOMO−1 → LUMO | 19.72% |
| | | | | HOMO → LUMO | 30.12% |
| | 2.5522 (486 nm) | 2 | 0.0029 | HOMO−1 → LUMO+1 | 21.76% |
| | | | | HOMO → LUMO+1 | 28.08% |

The absorbance wavelengths of these materials are more readily related to the observed colors of each material, respectively. The cocrystals with 3DMABA absorb mostly below 600 nm, and they appear red/orange to the naked eye. Similarly, cocrystals with 4ABA are yellow, and they all absorb light below 500 nm, which is consistent with expectations.

**Photoluminescence studies.** Photoluminescence (PL) spectra were collected using a Jobin-Yvon Fluoromax-2 with a xenon arc lamp source and photon-counting detection electronics. Although several compounds exhibited photoluminescence, the observed color did not originate from their emission. Instead, visible color arises solely from their absorption characteristics in the UV-visible range. The corresponding photoluminescence data are provided in the supporting information.

**Solid-state replacement studies.** The PXRD patterns of the ground products showed no significant differences from those of the parent cocrystals (SI). All characteristic peaks of the original cocrystal and the second coformer were retained, and no new peaks corresponding to a new phase were observed. These results indicate that solid-state interconversion has not occurred under the given conditions, even at a 1:1

 

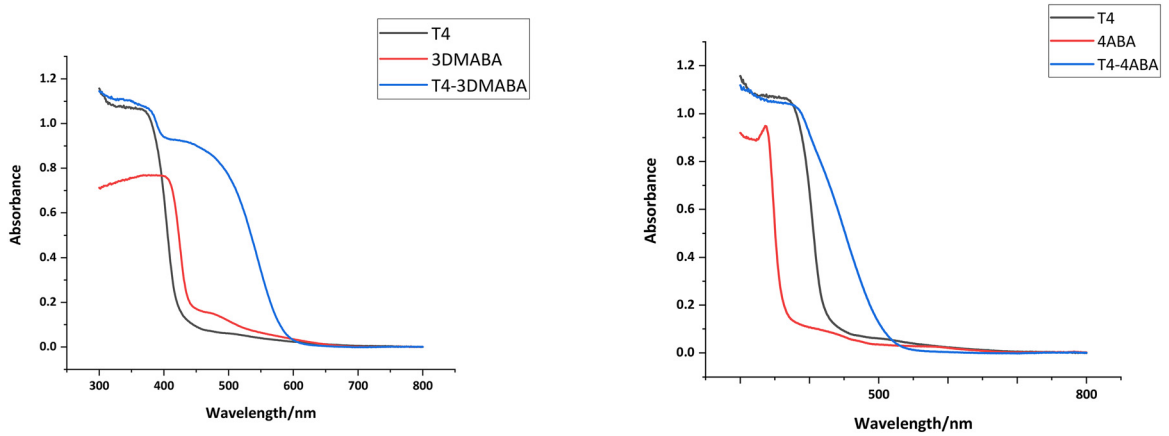


**Fig. 10** Solid-state UV-visible spectra comparison of (a) T4-3DMABA cocrystal with its parent materials and (b) T4-4ABA cocrystal with its parent materials.

stoichiometric ratio. This indicated that the initially formed cocrystal is likely thermodynamically stable and resistant to coformer replacement at least under the experimental conditions that we explored.

## Conclusions

In summary, nine cocrystals were successfully synthesized and fully characterized. By deliberately selecting coformers and systematically modifying the targets, we were able to maintain structural consistency across all cocrystals while preserving the $R_2^2(8)$ hydrogen-bonded motif. The crystal structure analysis reveals that the donor and acceptor molecules in each cocrystal are combined in a 1 : 1 stoichiometric ratio, except for T5-4ABA, which has a 2 : 1 acceptor : donor ratio. This demonstrates that competing intermolecular forces, such as sterics and hydrogen bonding, do not significantly restrict control over solid-state structural parameters.

All cocrystals exhibited color changes during liquid-assisted grinding. These cocrystals have small HOMO–LUMO gaps (2.6 eV for T2-3DMABA-PI; 2.5 eV for T3-3DMABA, T4-3DMABA, and T5-3DMABA; 3.3 eV for T2-4ABA and T3-4ABA; 3.5 eV for T4-4ABA; and 3.1 eV for T5-4ABA), which facilitates charge-transfer and serves as a rationale for their observed colors. This indicates that calculated HOMO–LUMO gaps of donor-acceptor pairs can be used to guide the design of functional cocrystals with desired colors.

In solid-state UV-visible spectra, the absorption bands of all cocrystals display considerable broadening and red shift, indicating the occurrence of charge-transfer between the acceptor and the donor molecules within the cocrystals. Photoluminescence studies showed that only some compounds are photoluminescent; however, the observed colors arise solely from UV-visible absorption.

Overall, this study shows that systematic coformer selection enables modulation of photophysical properties and establishes a predictive strategy for the rational design of functional cocrystal systems.

## Conflicts of interest

There are no conflicts to declare.

## Data availability

Supplementary information (SI): the following support information is available free of charge. Crystallographic data, FTIR spectra, PXRD patterns, solid-state UV-vis spectra and photoluminescence spectra. See DOI: https://doi.org/10.1039/d6ce00063k.

CCDC 2518010–2518018 contain the supplementary crystallographic data for this paper.[64a–i]

## Acknowledgements

The authors would like to acknowledge NSF-MRI Grant CHE-2018414, which was used to purchase the Rigaku XtaLAB Synergy-S single-crystal X-ray diffractometer and the associated software employed in this study, and the Johnson Cancer Research Center for providing funding. The authors would like to acknowledge Dr. Jun Li for providing access to the solid-state UV-vis absorption instrument and Mr. Zahirul Saddam for operating the instrument and collecting the data. The authors also thank Dr. Daniel Higgins and Ms. Sorour Salehi for their support with the photoluminescence experiments. The authors further acknowledge Mr. Sulalith Samarasinghe for helpful discussions and guidance regarding the theoretical calculations.

## References

1 G. Barra, L. Guadagno, M. Raimondo, M. Gabriella Santonicola, E. Toto and S. V. Ciprioti, *Polymer*, 2023, **15**, 3786–3786.

2 M. Rahban, S. Zolghadri, N. Salehi, F. Ahmad, T. Haertlé, N. Rezaei-Ghaleh, L. Sawyer and A. A. Saboury, *Int. J. Biol. Macromol.*, 2022, **214**, 642–654.

3 M. Svärd, D. Ahuja and Å. C. Rasmuson, *Cryst. Growth Des.*, 2020, **20**, 4243–4251.
4 H. D. Clarke, K. K. Arora, H. M. Bass, P. Kavuru, T. T. Ong, T. Pujari, Ł. Wojtas and M. J. Zaworotko, *Cryst. Growth Des.*, 2010, **10**, 2152–2167.
5 M. Oja, S. Sild, G. Piir and U. Maran, *Pharmaceutics*, 2022, **14**, 2248.
6 A. Izuren, M. T. Bakhtiar, S. A. Rahim, F. Adam, W. H. Danial and M. R. Abu Bakar, *J. Pharm.*, 2025, **5**, 170–185.
7 M. Wang, H. Zhang, X. Li, B. Zhu, G.-B. Ren, M.-H. Qi, Z. Li and X. Xu, *Cryst. Growth Des.*, 2025, **25**, 6636–6655.
8 W. Wu, Z. Wei, J. Wang, J. Shang, M. Wang, S.-S. Chi, Q. Wang, L. Du, T. Zhang, Z. Zheng and Y. Deng, *Chem. Eng. J.*, 2021, **424**, 130335.
9 Z. Wang, W. Han, R. Shi, X. Han, Y. Zheng, J. Xu and X.-H. Bu, *JACS Au*, 2024, **4**, 279–300.
10 K. Chen, W. Wu, H. Zhao, Y. Wei, S. Zhu, X. Huang, N. Wang, T. Wang and H. Hao, *Cryst. Growth Des.*, 2023, **23**, 8637–8645.
11 G. Wei, P. Chen, J. Wu, Y. Liang, J. Li, H. Huang, Z. Lan, X. Liang, W. Zhou, P. Qing and S. Tang, *ChemPhysChem*, 2024, **26**, e202400957–e202400957.
12 A. Mohammad, T. Köhler, S. Biswas, H. Stöcker and D. C. Meyer, *ACS Appl. Energy Mater.*, 2023, **6**, 2914–2923.
13 M. T. Agne, T. Böger, T. Bernges and W. G. Zeier, *PRX Energy*, 2022, **1**, 031002.
14 C. B. Aakeröy, J. Desper, M. Fasulo, I. Hussain, B. Levin and N. Schultheiss, *CrystEngComm*, 2008, **10**, 1816.
15 Y. Liu, L. Wang, L. Zhao, Y. Zhang, Z.-T. Li and F. Huang, *Chem. Soc. Rev.*, 2024, **53**, 1592–1623.
16 T. Steiner, *Angew. Chem., Int. Ed.*, 2002, **41**, 48–76.
17 I. Hisaki, Y. Suzuki, E. Gomez, Q. Ji, N. Tohnai, T. Nakamura and A. Douhal, *J. Am. Chem. Soc.*, 2019, **141**, 2111–2121.
18 A. A. Marasinghe, B. B. Averkiev and C. B. Aakeröy, *CrystEngComm*, 2025, **27**, 7000–7011.
19 H. Wang, H. K. Bisoyi, A. M. Urbas, T. J. Bunning and Q. Li, *Chem. – Eur. J.*, 2018, **25**, 1369–1378.
20 L. Meazza, J. A. Foster, K. Fucke, P. Metrangolo, G. Resnati and J. W. Steed, *Nat. Chem.*, 2012, **5**, 42–47.
21 P. Scilabra, G. Terraneo and G. Resnati, *Acc. Chem. Res.*, 2019, **52**, 1313–1324.
22 L. Vogel, P. Wonner and S. M. Huber, *Angew. Chem., Int. Ed.*, 2018, **58**, 1880–1891.
23 M. Jiang, C. Zhen, S. Li, X. Zhang and W. Hu, *Front. Chem.*, 2021, **9**, 764628.
24 Y. Ding, Y. Zhao and Y. Liu, *Aggregate*, 2024, **5**, e626.
25 D. D. Chavan, V. M. Thorat, A. S. Shete, R. R. Bhosale, S. J. Patil and D. D. Tiwari, *Cureus*, 2024, **16**(9), e70328.
26 A. Raheem Thayyil, T. Juturu, S. Nayak and S. Kamath, *Adv. Pharm. Bull.*, 2020, **10**, 203–212.
27 Y. Chen, M. Zhuo, X. Wen, W. Chen, K. Zhang and M. Li, *Adv. Sci.*, 2023, **10**, 2206830.
28 A. Garai and K. Biradha, *Cryst. Growth Des.*, 2020, **20**, 8059–8070.
29 J. Guo, L. Xu, M. Cai, Z. Dong, Q. Mu, X. Wang, H. Fan, F. Teng, X. He, H. Jiang and P. Hu, *Cryst. Growth Des.*, 2024, **24**, 1293–1301.
30 X.-X. Liu, P. Shi, X.-L. Dai, Y.-L. Huang, T.-B. Lu and J.-M. Chen, *CrystEngComm*, 2022, **24**, 8449–8456.
31 W. Xu, G. Huang, Z. Yang, Z. Deng, C. Zhou, J.-A. Li, M.-D. Li, T. Hu, B. Z. Tang and D. L. Phillips, *Nat. Commun.*, 2024, **15**, 2561.
32 W. Yao, P. Wu, Y. Xie, X. Shen, S. Xia and L. Yu, *CrystEngComm*, 2024, **26**, 2155–2165.
33 M. R. Dhondale, P. Thakor, A. G. Nambiar, M. Singh, A. K. Agrawal, N. R. Shastri and D. Kumar, *Pharmaceutics*, 2023, **15**, 189.
34 A. Chettri, A. Subba, G. Singh and P. P. Bag, *J. Pharm. Pharmacol.*, 2023, **76**, 1–12.
35 K. C. Waterman, A. K. Waterman, T. M. Botoy, J. Li, F. Qiu and M. Hawley, *Pharm. Dev. Technol.*, 2021, **26**, 1130–1135.
36 M. Singh, M. P. Sawarkar, M. R. Dhondale, D. R. Serrano, A. K. Agrawal and D. Kumar, *Cryst. Growth Des.*, 2025, **25**, 7852–7868.
37 A. Alvani and A. Shayanfar, *Cryst. Growth Des.*, 2022, **22**, 6323–6337.
38 R. Thakuria, A. Delori, W. Jones, M. P. Lipert, L. Roy and N. Rodríguez-Hornedo, *Int. J. Pharm.*, 2013, **453**, 101–125.
39 S. P. Gopi, M. Banik and G. R. Desiraju, *Cryst. Growth Des.*, 2016, **17**, 308–316.
40 M. Przybyłek, D. Ziółkowska, K. Mroczyńska and P. Cysewski, *Cryst. Growth Des.*, 2017, **17**, 2186–2193.
41 C. B. Aakeröy, S. Forbes and J. Desper, *J. Am. Chem. Soc.*, 2009, **131**, 17048–17049.
42 C. C. Sun and H. Hou, *Cryst. Growth Des.*, 2008, **8**, 1575–1579.
43 P. Sanphui, M. K. Mishra, U. Ramamurty and G. R. Desiraju, *Mol. Pharmaceutics*, 2015, **12**, 889–897.
44 S. Karki, T. Friščić, L. Fábián, P. R. Laity, G. M. Day and W. Jones, *Adv. Mater.*, 2009, **21**, 3905–3909.
45 M. Guo, X. Sun, J. Chen and T. Cai, *Acta Pharm. Sin. B*, 2021, **11**, 2537–2564.
46 A. Yadav, A. Shete, A. Dabke, P. Kulkarni and S. Sakhare, *Indian J. Pharm. Sci.*, 2009, **71**, 359.
47 E. Stoler and J. Warner, *Molecules*, 2015, **20**, 14833–14848.
48 L. Sun, W. Zhu, X. Zhang, L. Li, H. Dong and W. Hu, *J. Am. Chem. Soc.*, 2021, **143**, 19243–19256.
49 C. B. Aakeröy and D. J. Salmon, *CrystEngComm*, 2005, **7**, 439.
50 C. B. Aakeröy and P. D. Chopade, Cocrystals: Synthesis, Structure, and Applications, in *Supramolecular Chemistry*, ed. P. A. Gale and J. W. Steed, 2012, DOI: 10.1002/9780470661345.smc113.
51 C. A. Gunawardana and C. B. Aakeröy, *Chem. Commun.*, 2018, **54**, 14047–14060.
52 K. Zheng, S. Gao, M. Chen, A. Li, W. Wu, S. Qian and Q. Pang, *CrystEngComm*, 2020, **22**, 1404–1413.
53 Y. Wang, H. Wu, L. O. Jones, M. A. Mosquera, C. L. Stern, G. C. Schatz and J. F. Stoddart, *J. Am. Chem. Soc.*, 2023, **145**, 1855–1865.
54 J. R. G. Sander, D.-K. Bučar, R. F. Henry, J. Baltrusaitis, G. G. Z. Zhang and L. R. Macgillivray, *J. Pharm. Sci.*, 2010, **99**, 3676–3683.

 

55 A. M. Abeysekera, A. S. Sinha and C. B. Aakeroy, *Molecules*, 2021, **26**, 1147.
56 J. A. Bis and M. J. Zaworotko, *Cryst. Growth Des.*, 2005, **5**, 1169–1179.
57 M. Hemamalini, W.-S. Loh, C. K. Quah and H.-K. Fun, *Chem. Cent. J.*, 2014, **8**, 31.
58 A. A. Marasinghe, B. B. Averkiev and C. B. Aakeröy, *Cryst. Growth Des.*, 2025, **25**, 8703–8711.
59 *Spartan'14*, Wavefunction, Inc., Irvine, CA, USA, 2014.
60 O. V. Dolomanov, L. J. Bourhis, R. J. Gildea, J. A. K. Howard and H. Puschmann, *J. Appl. Crystallogr.*, 2009, **42**, 339–341.
61 I. Usón and G. M. Sheldrick, *Acta Crystallogr., Sect. D:Struct. Biol.*, 2018, **74**, 106–116.
62 C. F. Macrae, I. Sovago, S. J. Cottrell, P. T. A. Galek, P. McCabe, E. Pidcock, M. Platings, G. P. Shields, J. S. Stevens, M. Towler and P. A. Wood, *J. Appl. Crystallogr.*, 2020, **53**, 226–235.
63 G. M. Sheldrick, *Acta Crystallogr., Sect. A:Found. Adv.*, 2015, **71**, 3–8.
64 (*a*) CCDC 2518010: Experimental Crystal Structure Determination, 2026, DOI: 10.5517/ccdc.csd.cc2qj64m; (*b*) CCDC 2518011: Experimental Crystal Structure Determination, 2026, DOI: 10.5517/ccdc.csd.cc2qj65n; (*c*) CCDC 2518012: Experimental Crystal Structure Determination, 2026, DOI: 10.5517/ccdc.csd.cc2qj66p; (*d*) CCDC 2518013: Experimental Crystal Structure Determination, 2026, DOI: 10.5517/ccdc.csd.cc2qj67q; (*e*) CCDC 2518014: Experimental Crystal Structure Determination, 2026, DOI: 10.5517/ccdc.csd.cc2qj68r; (*f*) CCDC 2518015: Experimental Crystal Structure Determination, 2026, DOI: 10.5517/ccdc.csd.cc2qj69s; (*g*) CCDC 2518016: Experimental Crystal Structure Determination, 2026, DOI: 10.5517/ccdc.csd.cc2qj6bt; (*h*) CCDC 2518018: Experimental Crystal Structure Determination, 2026, DOI: 10.5517/ccdc.csd.cc2qj6dw; (*i*) CCDC 2518017: Experimental Crystal Structure Determination, 2026, DOI: 10.5517/ccdc.csd.cc2qj6cv.